Effect of Strength Anisotropy on Strain Localization in Natural Clay

Shiyi Liu [1, 2], Zhiwei Gao [2], Ming Li [1]

[1] *School of Resources and Civil Engineering, Northeastern University, Shenyang 110819, China*

[2] *James Watt School of Engineering, University of Glasgow, Glasgow G12 8QQ, UK*

Corresponding author: Shiyi Liu, Email: liu-shiyi@hotmail.com

Shiyi Liu, Orcid: https://orcid.org/0000-0001-7853-8837

Zhiwei Gao, Orcid: https://orcid.org/0000-0002-5501-9855

Ming Li, Orcid: https://orcid.org/0000-0002-7704-3856

Abstract

Strain localization in soils causes the failure of slopes and foundations. Shear strength is an important factor that affects strain localization in soils. It is well known that the shear strength of natural clay is highly anisotropic due to the internal soil structure. An anisotropic failure criterion for natural clay is presented in which an anisotropic variable is used to describe the relative orientation between the stress directions and soil fabric. The failure criterion is employed in a Drucker–Prager model that considers the strain-softening of natural clay. The effect of anisotropic strength on strain localization in clay is analyzed by two examples, including an undrained slope stability analysis and a simulation of a hollow cylinder test of Boom clay. It is found that the shear strength anisotropy affects both the strain localization pattern and factor of safety for the undrained slope. Simulation of the tests on Boom clay shows that the model with the anisotropic yield criterion yields an eye-shaped strain localization pattern that cannot be obtained by the model with the isotropic yield criterion.

Keywords: Anisotropic strength, Natural clay, Strain localization, Drucker–Prager (DP) model, Slope stability, Boom clay

1 Introduction

Strain localization, such as shear band development, causes the failure of slopes and foundations. Strain localization is affected by many factors [62, 40, 51]. Among them, the shear strength is one of the most important. Natural clays always have an anisotropic internal structure or fabric (e.g., particle orientation and void space distribution) that is caused by compaction or gravity [61, 54], which results in inherent anisotropy. This makes the shear strength of natural clay dependent on the loading direction [39] and the degree of saturation [30, 31]. Another kind of anisotropy is caused by loading history, called stress-induced anisotropy or induced anisotropy. The inherent anisotropy is addressed in this paper. Existing research has shown that the location of the slip surfaces and the factor of safety of a clay slope are significantly affected by strength anisotropy [55]. A significantly lower factor of safety will be obtained when strength anisotropy is considered. Furthermore, strain localization in Boom clay due to excavation is found to be influenced by strength anisotropy [20].

An anisotropic model is thus crucial for constitutive modelling in clays. The key feature of the anisotropic model is to use an anisotropic yield criterion for the modelling of inherent anisotropy and to incorporate a kinematic hardening law for the modelling of induced anisotropy [66]. Another attractive alternative to the kinematic hardening method is the micromechanics approach [67, 68, 66]. Rotated yield surfaces have been widely used in modelling the anisotropic behaviour of clay [2, 12, 13, 35, 63, 64, 69]. This approach is effective for modelling the anisotropy caused by the previous loading history. The evolution of anisotropy can be easily considered in the modelling framework. However, when the initial effective stress state is isotropic, the soil fabric is typically assumed to be isotropic as well, which may not be reasonable for natural clay.

There have been several methods where inherent anisotropy was incorporated into the constitutive description [19, 53, 72]. One of the most important ways is to construct anisotropic models based on the existing isotropic criteria, such as the von Mises criterion [29], the Mohr–Coulomb criterion [48], the Cam-Clay model [45] and the modified Cam-Clay model [11].

To model the inherent anisotropy of natural clays, Casagrande and Carillo [8] presented an expression for the anisotropic undrained shear strength of clay, in which the direction of the major principal stress is needed. While this expression has been validated by the test results of some soils, such as Canadian Welland clay [43], it can only be used when the bedding plane is horizontal. Furthermore, Grimstad et al. [28] proposed an anisotropic Tresca model for describing the undrained response of clays, i.e., NGI-ADP. Krabbenhøft et al. [37] developed the AUS model following the works of Grimstad et al. [28]. This model includes three undrained shear strength parameters obtained by three sets of tests, including triaxial extension, triaxial compression, and simple shear. However, all these tests must be performed on a soil sample with a horizontal bedding plane. The model parameters will have to be adjusted when the bedding plane orientation is not horizontal in a real application. An anisotropic modified Cam-Clay model was proposed to describe the anisotropy of rock, which involves the microstructure tensor [53, 6, 72, 73]. It is denoted by a second-order tensor, which is the tensor product of the unit normal vector to the bedding plane and itself. Methods using fabric tensors have also been developed to model the strength anisotropy of soils. In these methods, joint invariants of the stress tensor and fabric tensor are needed in the formulations [14, 49, 46]. For instance, Gao et al. [22] developed an anisotropic model for soils based on the works of Yao et al. [65] and Dafalias et al. [14]. In this model, an anisotropic variable that describes the relative orientation between the loading direction and the material fabric is introduced. This model has been used for both soils and rocks.

Some of the models have been used in modelling strain localization in clay. The NGI-ADPSoft model based on NGI-ADP, which takes into account the strain-softening behaviour of clays, has been used to analyze a full-scale railway embankment built on a soft clay deposit [15]. Based on the method of Pietruszczak and Mroz [49], Tang et al. [59] proposed a failure criterion in the form of Casagrande's expression [8] to present an anisotropic DP model and conducted a simulation of strain localization in an undrained slope of clay. However, the failure criterion in this study lacks variety and is not applicable. In Belgium, Switzerland and France, Boom clay, Opalinus clay and Callovo-Oxfordian clay are candidate host rocks for the deep geological disposal of radioactive waste. Strain localization in these clays has been studied [20, 5, 47, 44]. In the study of Mánica et al. [44], a four-parameter complex anisotropic failure criterion proposed by Conesa et al. [10] using a curve-fitting approach was used. However, none of these studies attempts to construct a "complete" anisotropic constitutive model but dynamically updates the anisotropic cohesion and calculates the direction of the major principal stress in nonlinear incremental iterative calculations. In other words, the gradient of the yield function of the constitutive model does not include a component of anisotropic cohesion. Excessive load increments can affect the accuracy of describing cohesion [16].

In this study, an elastoplastic DP model is proposed that considers the anisotropic strength as well as strain-hardening/softening characteristics of clay. In the yield function, an anisotropic function of stress is used to describe the anisotropic strength of the clay. Since the shear strength is the focus of this study, the soil response is assumed to be purely elastic before failure. Under undrained conditions, the anisotropic DP model reduces to the anisotropic von Mises model. The model is implemented in the user subroutines of ABAQUS software [1]. The validation of the proposed anisotropic DP model is demonstrated by two typical examples, undrained slope stability analysis and simulation of the Boom clay hollow cylinder test, representing limit equilibrium and progressive failure problems, respectively. The effect of anisotropic strength on strain localization in clay is analyzed with emphasis.

2 Anisotropic plastic constitutive model

2.1 Anisotropic failure criterion

The cross-anisotropy of clays can be characterized by the symmetric second-order fabric tensor F_{ij} [46].

$$F_{ij} = \begin{bmatrix} F_x & 0 & 0 \\ 0 & F_y & 0 \\ 0 & 0 & F_z \end{bmatrix} = \frac{1}{3+\Delta}\begin{bmatrix} 1+\Delta & 0 & 0 \\ 0 & 1-\Delta & 0 \\ 0 & 0 & 1+\Delta \end{bmatrix} \tag{1}$$

where Δ is a scalar and $0 < \Delta < 1$. It is assumed that the principal directions of the fabric tensor are consistent with the local coordinate system (x, y, z) and that the x-z plane is the isotropic plane, as shown in Fig. 1. The global coordinate axes are the x_i, y_i and z_i axes. It is worth noting that the isotropic plane is not necessarily horizontal.

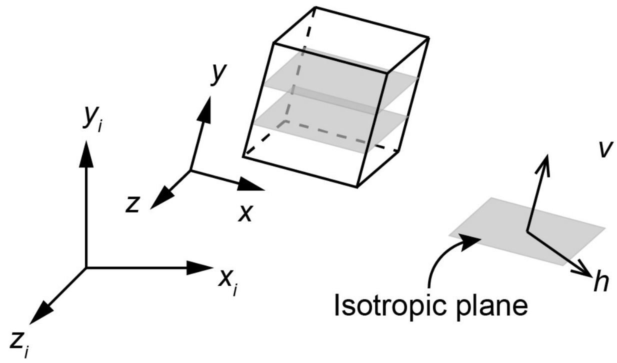

Fig. 1. Schematic diagram of the local coordinate system and the isotropic plane of the clay.

The strength of clay depends on the soil structure in clay and the loading direction. Gao and Zhao [23] proposed an anisotropic function $g(A)$ (Eq. (2)) to describe the anisotropic strength of geomaterials.

$$g(A) = \exp\left[\sum_{i=1}^{n} e_i (1+A)^i\right] \tag{2}$$

where e_i is a set of material parameters. For isotropic soil, $e_i = 0$. A is the anisotropic state variable. Based on the deviatoric stress tensors s_{ij} and the deviatoric part of the fabric tensor d_{ij}, the variable A can be expressed as

$$A = \frac{s_{ij} d_{ij}}{\sqrt{s_{mn} s_{mn}}\sqrt{d_{mn} d_{mn}}} = \frac{s_x - 2s_y + s_z}{2q} \tag{3}$$

where $d_{ij} = F_{ij} - F_{kk}\delta_{ij}/3$, and q is the equivalent von Mises stress:

$$q = \sqrt{\frac{3}{2} s_{ij} s_{ij}} \tag{4}$$

where s_{ij} is the deviatoric stress tensor and s_x, s_y and s_z are deviatoric stresses in the three-axis directions of the local coordinate system. It is worth noting that the normalized deviatoric fabric tensor, i.e., Eq. (5) is just a constant diagonal matrix. Therefore, the microscopic parameter Δ is not required in the numerical simulation.

$$\frac{d_{ij}}{\sqrt{d_{mn}d_{mn}}} = \frac{1}{\sqrt{6}}\begin{bmatrix} 1 & 0 & 0 \\ 0 & -2 & 0 \\ 0 & 0 & 1 \end{bmatrix} \tag{5}$$

In the proposed model, the anisotropic function $g(A)$ is used to define the anisotropic strength of clays, and $n = 3$. To illustrate how to determine the parameters e_1, e_2 and e_3, the hollow cylinder torsional shear test under undrained conditions on Gault clay in the UK [7] is taken as an example. In Fig. 2, α is the angle between the major principal stress and the axis of the isotropic plane. S_u is the peak undrained shear strength of Gault clay for various α and $S_u = g(A)S_{u0}$, where S_{u0} is the undrained shear strength at $\alpha = 0°$.

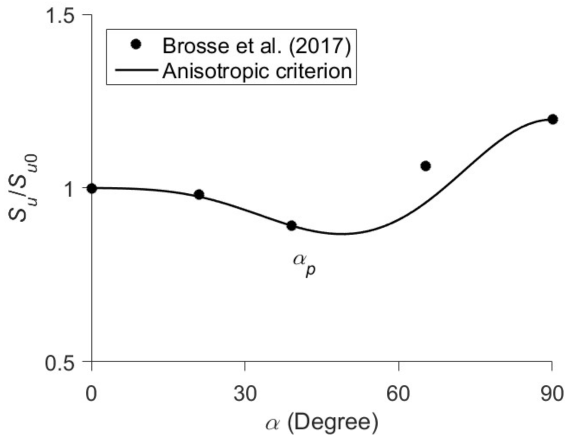

Fig. 2. Comparison between the data of the torsional test on Gault clay [7] and the proposed anisotropic failure criterion.

For the hollow cylinder torsional shear test, the formula $A^{(\alpha)}$ has been given [23]. $A^{(\alpha)}$ is used to determine the anisotropic parameters e_1, e_2, and e_3, then Eq. (3) with e_1, e_2, and e_3 is adopted in the numerical simulation.

$$A^{(\alpha)} = \frac{-3\cos^2\alpha + b + 1}{2\sqrt{b^2 - b + 1}} \tag{6}$$

where b is the intermediate principal stress ratio expressed as

$$b = \frac{\sigma_2 - \sigma_3}{\sigma_1 - \sigma_3} \tag{7}$$

σ_1, σ_2, and σ_3 are the major, intermediate, and minor principal stresses, respectively. The test results for Gault clay consist of five data points, of which the first ($\alpha = 0°$), third ($\alpha_p = 39°$), and fifth points ($\alpha = 90°$) are chosen to determine e_1, e_2, and e_3 by solving Eqs. (8) with $b = 0.5$. Note that b is a constant in all the tests.

$$\begin{cases} e_1\left(1 + A^{(0)}\right) + e_2\left(1 + A^{(0)}\right)^2 + e_3\left(1 + A^{(0)}\right)^3 = \ln K^{(0)} = 0 \\ e_1\left(1 + A^{(90°)}\right) + e_2\left(1 + A^{(90°)}\right)^2 + e_3\left(1 + A^{(90°)}\right)^3 = \ln K^{(90°)} \\ e_1\left(1 + A^{(\alpha_p)}\right) + e_2\left(1 + A^{(\alpha_p)}\right)^2 + e_3\left(1 + A^{(\alpha_p)}\right)^3 = \ln K^{(\alpha_p)} \end{cases} \tag{8}$$

where

$$K^{(\alpha)} = g\left(A^{(\alpha)}\right) = \frac{S_u}{S_{u0}} \tag{9}$$

The prediction of the anisotropic failure criterion is shown in Fig. 2.

2.2 Anisotropic DP Yield Function and Potential Function

In Fig. 3, the isotropic linear DP yield criterion for clays in terms of effective stresses [17] is expressed as

$$F(p', q) = q - m\left(p' + \frac{c'}{\tan\varphi'}\right) = 0 \tag{10}$$

where

$$m = \frac{6\mathrm{si}\quad '}{3-\sin\quad '} \tag{11}$$

where φ' and c' are the effective internal friction angle and the effective cohesion, respectively. p' is the mean effective stress.

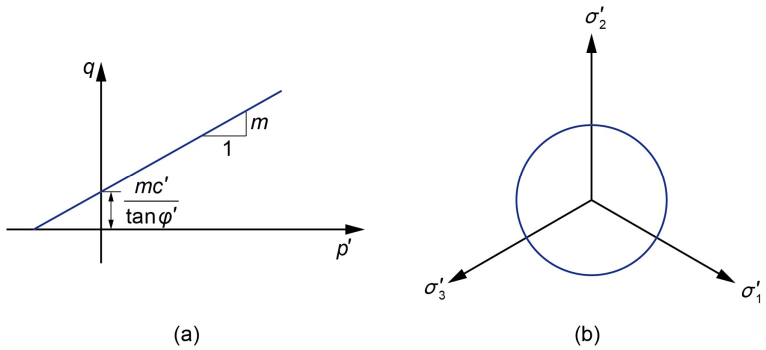

Fig. 3. Linear DP yield surface in (a) the meridional plane and (b) the deviatoric plane.

There are two strength parameters in the DP yield criterion, i.e., internal friction angle and cohesion. Duncan and Seed [18] and Sergeyev et al. [54] concluded that the internal friction angle of clay shows only moderate anisotropy and is independent of the loading direction. However, the undrained shear strength and cohesion are highly anisotropic. Therefore, anisotropic DP yield criteria considering only cohesive anisotropy have been frequently used [20, 59, 60]. To describe the anisotropic shear strength of clays under drained conditions, the proposed anisotropic DP yield function is written as

$$F(p', q, A) = q - m\left(p' + \frac{g(A)c_0'}{\tan\varphi'}\right) = 0 \tag{12}$$

where c_0' is the effective cohesion measure in triaxial compression with the direction of the major principal stress parallel to the axis of the isotropic plane.

Under undrained conditions, $\varphi' = 0$ and $S_{u0} = c_0'$ are assumed, and the DP yield function reduces to the von Mises yield function. Under plane strain conditions [1], the DP yield function is expressed as

$$F(q, A) = q - \sqrt{3}S_{u0}g(A) = 0 \tag{13}$$

where S_{u0} is the undrained shear strength when the direction of the major principal stress is parallel to the axis of the isotropic plane of the clay.

The plastic potential function G of the proposed model is written as

$$G = q - m'p' = 0 \tag{14}$$

where

$$m' = \frac{6\sin\psi}{3-\sin} \tag{15}$$

where ψ is the dilation angle. The gradient of the proposed anisotropic yield function is introduced in Appendix 1. Since the plastic potential function does not include the fabric tensor F_{ij}, the flow rule is noncoaxial [71, 24].

2.3 Hardening law and nonlocal strain-softening

Strain localization is usually simulated by the plastic model with strength parameters that decrease linearly or nonlinearly with increasing equivalent plastic strain [32, 33, 36]. In the proposed model, the isotropic strain-hardening/softening law of clay is a function of the equivalent plastic strain ε_{dp}.

$$\varepsilon_{dp} = \int_0^t \sqrt{\frac{2}{3}\dot{\boldsymbol{e}}:\dot{\boldsymbol{e}}}\,dt \tag{16}$$

where $\dot{\boldsymbol{e}}$ is the rate tensor of the deviatoric plastic strain and t is the time of the simulation.

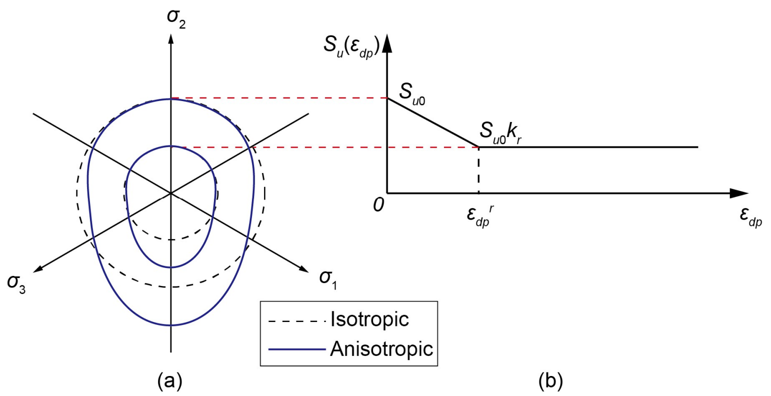

Fig. 4. Isotropic strain-softening law and changes in (a) yield surface and (b) relation between undrained shear strength and the equivalent plastic strain.

The simplest softening law is a linear relationship between the shear strength and the equivalent plastic strain, e.g., the one proposed by Potts et al. [50], as shown in Fig. 4 (b). In the analysis in Section 4.2, a nonlinear hardening/softening relationship is used. Based on the anisotropic parameters of Gault clay, the method proposed by

Gao and Zhao [23] is utilized to plot the yield surfaces in the deviatoric plane that change from a circle to an irregular ellipse due to the anisotropic function $g(A)$. The yield surface shape does not change but shrinks with increasing plastic strain (Fig. 4 (a)).

For simplicity, the anisotropy of undrained shear strength and the softening characteristics of cohesion are assumed to be independent. Therefore, in Fig. 5, the undrained shear strength can be illustrated as a function of the anisotropy parameters e_1, e_2, and e_3 and softening parameters k_r and ε_{dp}^{r}.

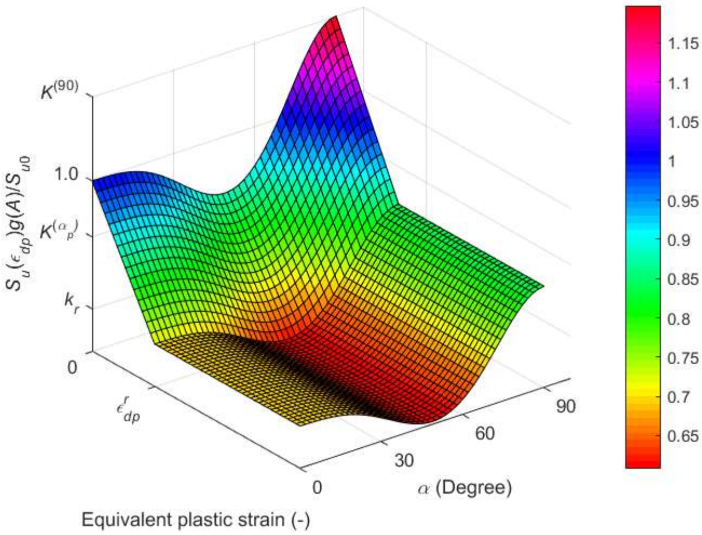

Fig. 5. Undrained strength as a function of the equivalent plastic strain and major principal stress direction α.

In finite element analysis (FEA), strain softening of the material results in mesh sensitivity. A partially nonlocal softening regularization approach proposed by Galavi and Schweiger [21] is employed to reduce the mesh sensitivity. In the approach, only the deviatoric strain is considered a nonlocal variable. A detailed introduction of the approach has been given [56, 57]. Following the implementation of the nonlocal approach proposed by Gao et al. [24], the nonlocal equivalent plastic strain at an integration point is expressed as

$$\varepsilon_{dp}^{*} = \frac{\sum_{i=1}^{N} (\varepsilon_{dp})_i \omega_i v_i}{\sum_{i=1}^{N} \omega_i v_i} \tag{17}$$

where N is the total number of integration points in the FEA. $(\varepsilon_{dp})_i$, v_i, and ω_i are the local equivalent plastic strain, volume, and weight function at the ith integration point, respectively. The weight function expressed below is used.

$$\omega_i = \frac{r_i}{l^2} \exp\left(-\frac{r_i}{l^2}\right) \tag{18}$$

where l is the internal length parameter and r_i is the distance between the current integration point and integration point i. Their units should be consistent with the units of the geometric dimensions of the model. To better describe the strain localization characteristics, the rate of the nonlocal equivalent plastic strain is given as

$$\dot{\varepsilon}_{dp}^{*}=\frac{\sum_{i=1}^{N}\left(\dot{\varepsilon}_{dp}\right)_{i}\omega_{i}v_{i}}{\sum_{i=1}^{N}\omega_{i}v_{i}} \tag{19}$$

3 Implementation of the Model

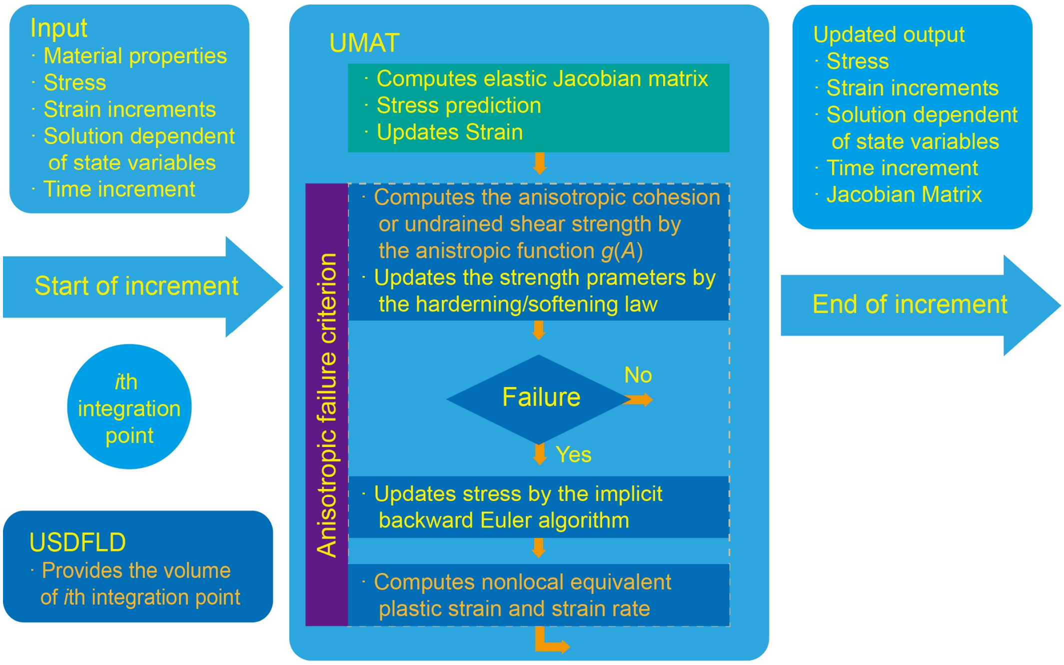

Fig. 6. Flow chart of the user subroutines for implementation of the proposed anisotropic DP model.

The proposed anisotropic DP model is implemented in the user subroutines of ABAQUS software [1]. Fig. 6 shows the flow chart of the user subroutines. The key parts of the code are the anisotropic yield criterion for clays and the nonlocal regularization approach. These two parts are implemented by the user subroutines to define a material's mechanical behaviour (UMAT) and to redefine field variables at an integration point (USDFLD). The stress integration algorithm for the constitutive model is the implicit backward Euler algorithm, which requires a Newton procedure to solve the nonlinear equations [3].

4 Strain Localization in Anisotropic Clay

To study the effect of anisotropic shear strength on the strain localization in natural clays, undrained slope stability analysis and simulation of the hollow cylinder test of Boom clay are chosen to represent the limit equilibrium problem and the progressive failure problem, respectively.

4.1 Stability analysis of undrained clay slope

There are two cases for stability analysis of undrained clay slopes. Case 1 is a stability analysis of an undrained clay slope with different anisotropic undrained shear strengths. Case 2 is a stability analysis of an undrained clay slope with different orientations of the bedding plane (i.e., isotropic plane), which might exist in naturally deposited clays owing to cross-bedding or postdepositional deformations. To better compare with the results in other literature, it is assumed that the potential function is consistent with the yield function in the proposed slope stability analysis.

4.1.1 Case 1: Slope with anisotropic undrained shear strengths

The cross-anisotropic shear strength relation for the undrained strength of clay proposed by Casagrande and Carillo [8] is expressed as

$$S_u = S_{u0}[K + (1 - K)\cos^2 \alpha] \quad (20)$$

where K is the ratio of the undrained shear strength at $\alpha = 90°$ to S_{u0}. For isotropic clays, $K = 1.0$. Lo (1965) found that Casagrande's expression is valid for the Welland clay in Canada. According to the cross-anisotropic strength relation, Chen et al. [9] proposed the upper bound (UB) method of limit analysis to evaluate the stability of anisotropic undrained slopes. Based on the proposed anisotropic DP model assuming ideal plasticity, the stability number N_s of the slope is calculated by the finite element strength reduction method (FESRM) [27, 42, 58] and is compared with the UB solution.

$$N_s = H_c\left(\frac{\gamma}{S_{u0}}\right) \quad (21)$$

where H_c is the critical height of the slope and γ is the unit weight of the clay.

Normally, the FESRM is used to solve the safety factor for a slope with a given height rather than solving the critical height and corresponding stability number of the slope. There is a relation between the safety factor and the stability number. In the FESRM, S_{u0} is used for the reduction, and the factor of safety F_s is expressed as

$$F_s = \frac{S_{u0}}{S_{u0}^f} \quad (22)$$

where S_{u0}^f is the factored shear strength parameter. Therefore,

$$N_s = H\left(\frac{\gamma}{S_{u0}^f}\right) = F_s H\left(\frac{\gamma}{S_{u0}}\right) \quad (23)$$

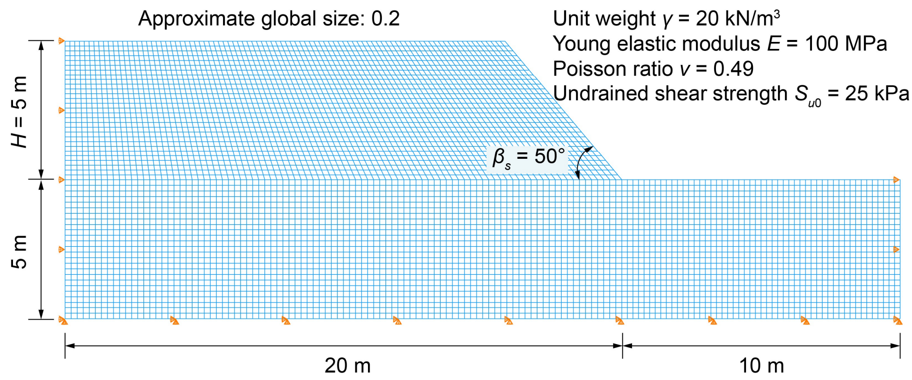

Fig. 7. The geometry, finite element mesh, boundary condition, and material parameters of the anisotropic undrained slope.

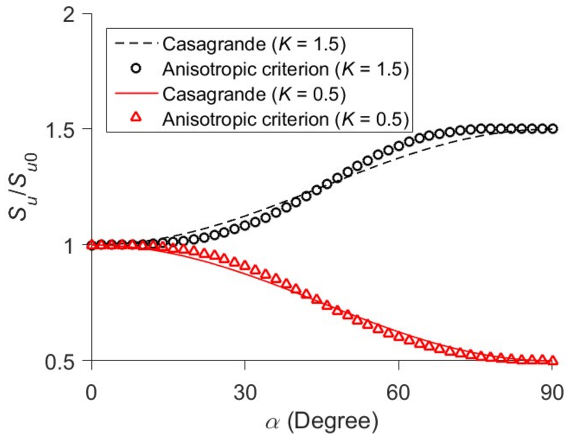

Fig. 8. Comparison between the criterion [8] and the proposed criterion for different K.

Taking the slope angle $\beta_s = 50°$ as an example, Fig. 7 presents the geometry, finite element mesh, boundary conditions, and material parameters of the example, assuming that the clay has isotropic elasticity. The initial stress is caused by gravity. Fig. 8 shows that there is little difference between the proposed anisotropic criterion and the Casagrande formula for $K = 1.5$ and 0.5. Kimmeridge clay [7] is a natural clay with $K > 1$. Table 1 lists the stability number of the undrained slope obtained by the UB and the FESRM with various K. When $K = 1.0$, the finite element limit equilibrium method (FELEM) [41] is used to validate the FESRM. The results obtained by the two finite element methods are close, with a percentage difference of only 3%. For $K < 1.0$, the stability number obtained by the FESRM is smaller than that obtained by the UB. This is because the UB result is an upper bound and the slip surface of the UB is a fixed logarithmic spiral. Moreover, the stability number obtained by the FESRM decreases with decreasing K. The percentage differences of the stability number obtained by the FESRM between $K = 0.5$ and $K = 1.5$ and $K = 0.5$ and $K = 1.0$ are 42% and 17%, respectively.

Table 1. Comparison of stability number with slope angle $\beta_s = 50°$.

K	N_s			Percentage difference from the FESRM (%)	
	Chen et al. [9] (UB)	FESRM	FELEM	UB	FELEM
1.5	-	6.48	-	-	-
1.4	-	6.21	-	-	-
1.3	-	6.05	-	-	-
1.2	-	5.80	-	-	-
1.1	-	5.56	-	-	-
1.0	5.68	5.33	5.47	7	3
0.9	5.58	5.16	-	8	-
0.8	5.47	5.00	-	9	-
0.7	5.37	4.85	-	11	-
0.6	5.27	4.71	-	12	-
0.5	5.16	4.57	-	13	-

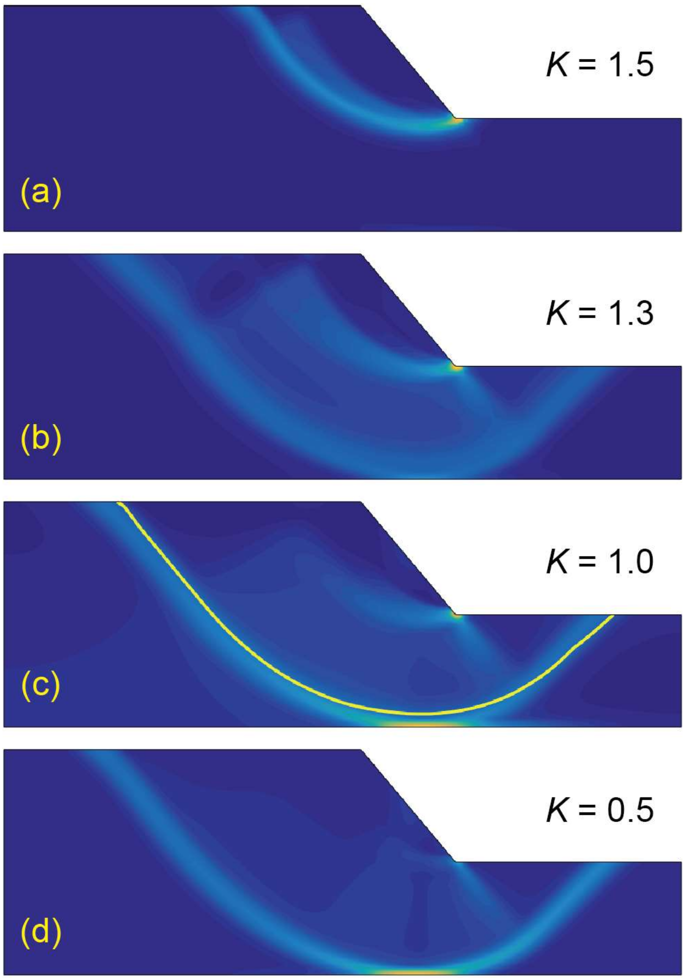

Fig. 9. Comparison of the slip surfaces obtained by the FESRM (contour of equivalent plastic strain) and FELEM (solid line).

In addition to the safety factor of the slope, the shape and location of the failure surface are also of great concern to geotechnical engineers or researchers. The equivalent plastic strain band (strain localization) across the slope is used as the criterion for the slope to reach the limit equilibrium state. In Fig. 9, a comparison of the slip surfaces obtained by the FELEM and FESRM with different K is given. At $K = 1.0$, both slip surfaces are close. When $K \leq 1.3$, the slip surface is a deep curved band. In contrast, when $K > 1.3$, the slip surface is a shallow curve band, which slides out from the toe of the slope.

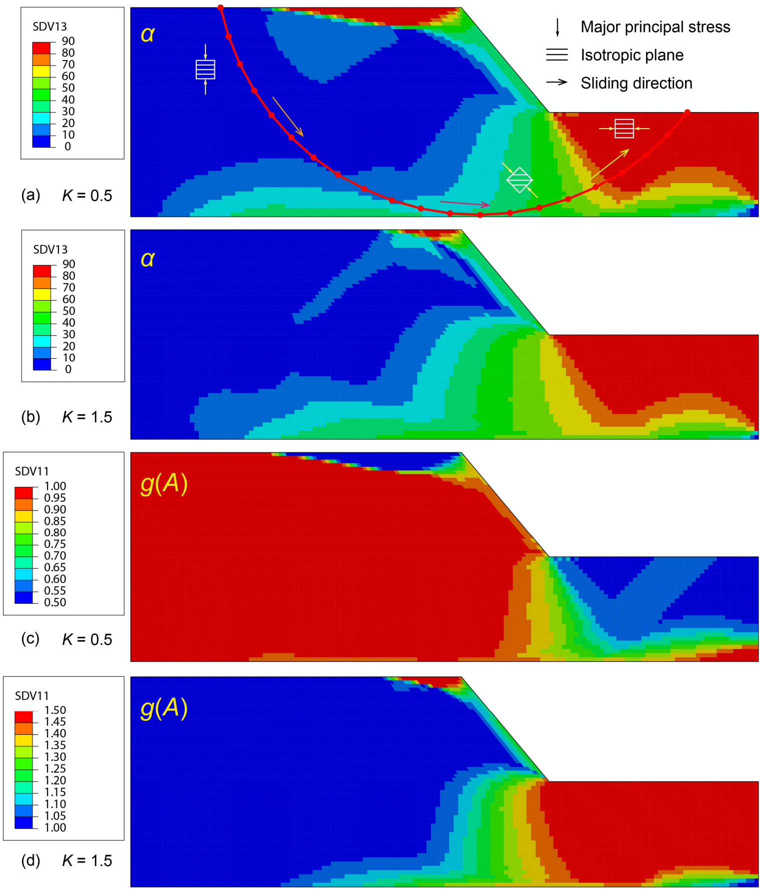

Fig. 10. Contours of the angle between the major principal stress and the axis of the isotropic plane at (a) $K = 0.5$ and (b) $K = 1.5$ and the comparison of the value of the anisotropic function $g(A)$ at (c) $K = 0.5$ and (d) $K = 1.5$.

Fig. 10 can be used to explain this difference. Fig. 10 (a) and (b) show the contours of the angle α in the cases of $K = 0.5$ and 1.5, and these two contours are similar. The angle α varies from zero to 90° along the sliding direction of the slip surface, i.e., the solid line in Fig. 10 (a). The value of the undrained shear strength changes with α. At $K = 0.5$ the strength increases with increasing angle α, while at $K = 1.5$, the strength decreases, as shown in Fig. 10 (c) and (d). When $K = 1.5$, the clay on the right side of the foundation provides higher resistance, so the slip surface is shallow.

4.1.2 Case 2: Slope with inclined bedding planes

Conesa et al. [10] proposed a complex cross-anisotropic failure criterion for the undrained strength of clay and analyzed undrained clay slopes with various bedding plane orientations. An inclined bedding plane may exist in a soil slope due to the loading history [25]. Taking Boston blue clay in the USA [52] as an example, the ratio of undrained shear strength is plotted in Fig. 11. The slope angle $\beta_s = 30°$ and other geometry, finite element mesh, boundary condition, and material parameters of the slope are the same as those in the last case. Fig. 11 also shows that the proposed anisotropic strength criterion and that of Conesa et al. can both capture the test data.

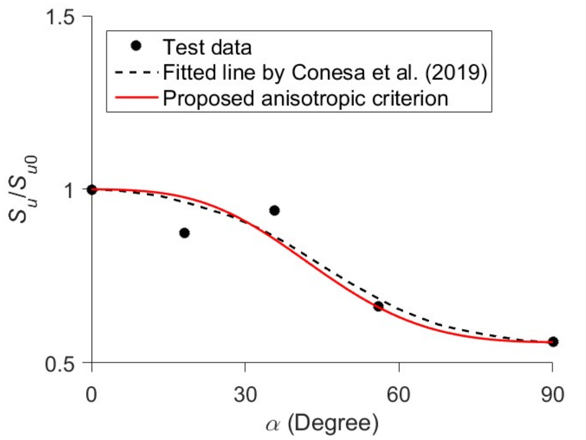

Fig. 11. Comparison between the test data of Boston clay [52] and the anisotropic strength criteria.

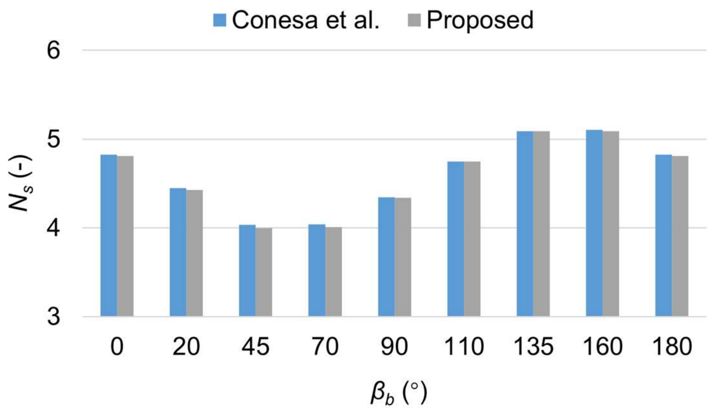

Fig. 12. Comparison of stability numbers with different β_b.

The orientation of the bedding plane is defined as the angle β_b between the tangent of the isotropic plane and the x-axis. Fig. 12 gives the stability numbers obtained by the proposed method and the method of Conesa et al. with different β_b. It shows that both results are close to each other. The angle β_b related to the maximum and minimum stability numbers should occur at approximately 135° and 45°, respectively. The difference between the maximum stability number and the minimum stability number is approximately 27%.

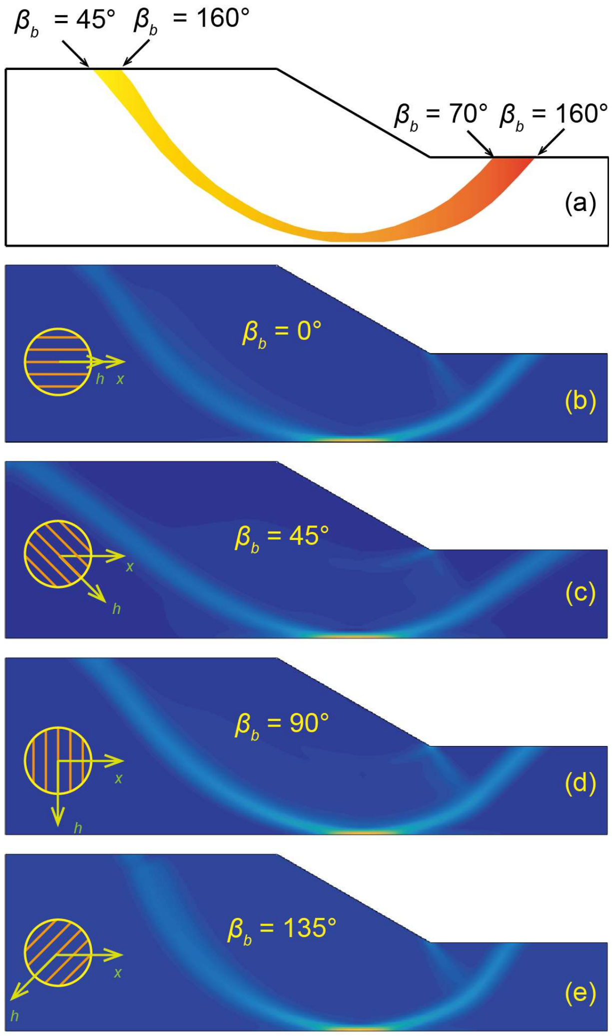

Fig. 13. Comparison between (a) the results from Conesa et al. [10] and (b)-(e) the slip surfaces obtained by the proposed method.

The slip surfaces obtained by the two methods are quite different, as shown in Fig. 13, although the stability numbers are consistent. Fig. 13 (a) shows the region consisting of all slip surfaces obtained by Conesa et al. with different β_b and angles corresponding to the entry and exit points of the slip surfaces. This reveals that in the analysis of Conesa et al., the shape and location of the slip surface are hardly affected by the bedding plane orientations. However, our analysis yields a different result in which there is an obvious difference among the slip surfaces. The angle β_b corresponding to the slip surface with lower curvature is 45° (Fig. 13 (c)), while the angle corresponding to the slip surface with higher curvature is 135° (Fig. 13 (e)). The slip surfaces are similar when $\beta_s = 0$ and 90° (Fig. 13 (b) and (d)). The essential difference between our undrained slope stability analysis and those from Conesa et al.

is whether the gradient of the yield function involves the component of the anisotropic undrained strength.

4.2 Simulation of the hollow cylinder test of Boom clay

In Belgium, Boom clay was selected as a candidate host formation for the disposal of high-level nuclear waste [4]. A set of Boom clay thick-walled hollow cylinder tests [38] reproduced the tunnel excavation in the host formation, approximated by reducing the internal confining pressure of the hollow cylinder specimen. Before and after unloading, the cross-section of the specimen was scanned by X-ray tomography, and the displacement of the tracking points within the cross-section was quantified. François et al. [20] established a hydromechanical constitutive model that can account for strain hardening/softening and elastic and plastic anisotropy to simulate the displacement of the tracking points in the hollow cylinder test. However, the major principal stress direction must be determined to obtain the drained shear strength.

Linear cross-anisotropic elastic Hooke’s law with five material parameters [26] is used to describe the elastic behaviour of boom clay, i.e., the relation of effective stress σ'_{ij} and strain ε_{ij}. E', v', and G in Eq.(24) are Young’s modulus, Poisson's ratio, and shear modulus. In the local Cartesian coordinate system (Fig. 1), the x-z plane is assumed to be an isotropic plane. If the clay is elastic isotropic, the elastic stress–strain relation reduces to Hooke’s law with two material parameters, i.e., E' and v'.

$$\begin{Bmatrix} \varepsilon_x \\ \varepsilon_y \\ \varepsilon_z \\ \gamma_{xy} \\ \gamma_{xz} \\ \gamma_{yz} \end{Bmatrix} = \begin{bmatrix} 1/E'_h & -v'_{vh}/E'_v & -v'_{hh}/E'_h & 0 & 0 & 0 \\ -v'_{vh}/E'_v & 1/E'_v & -v'_{vh}/E'_v & 0 & 0 & 0 \\ -v'_{hh}/E'_h & -v'_{vh}/E'_v & 1/E'_h & 0 & 0 & 0 \\ 0 & 0 & 0 & 1/G_v & 0 & 0 \\ 0 & 0 & 0 & 0 & 2(1+v'_{hh})/E'_h & 0 \\ 0 & 0 & 0 & 0 & 0 & 1/G_v \end{bmatrix} \begin{Bmatrix} \sigma'_x \\ \sigma'_y \\ \sigma'_z \\ \tau_{xy} \\ \tau_{xz} \\ \tau_{yz} \end{Bmatrix} \tag{24}$$

Fig. 14 shows the geometry, mesh, and boundary conditions of the hollow cylinder test. Under plane strain conditions, the pore water pressure and total pressure at the inner boundary gradually decrease and remain stable after 4200 s. Table 2 lists the geomechanical, hydraulic, and physical parameters of Boom clay [20]. Compared with the original parameters of Boom clay, the parameter values have not changed, but the expression has changed. For example, the anisotropy parameter K is used. The determination of e_1, e_2 and e_3 requires the results of a hollow cylinder torsional shear test, which increases the cost of parameter identification. Optimization-based parameter identification [34, 70] makes it possible to identify these parameters that come only from triaxial tests. For comparison with the same material parameters, e_1, e_2 and e_3 are determined by the test results of the triaxial tests. According to the original values of the anisotropic cohesion and Eqs. (6) and (8), the predicted shear strength of Boom clay is plotted in Fig. 15. The hardening behaviour of the internal friction angle and softening behaviour of cohesion are described by Eq. (25) [20] and plotted in Fig. 16.

$$\begin{cases} c'(\varepsilon_{dp}) = c'_0 + \frac{\varepsilon_{dp}}{B_S+\varepsilon_{dp}} c'_0(k_r - 1), \text{Softening} \\ \varphi'(\varepsilon_{dp}) = \varphi'_0 + \frac{\varepsilon_{dp}}{B_H+\varepsilon_{dp}} \varphi'_0(k_p - 1), \text{Hardening} \end{cases} \tag{25}$$

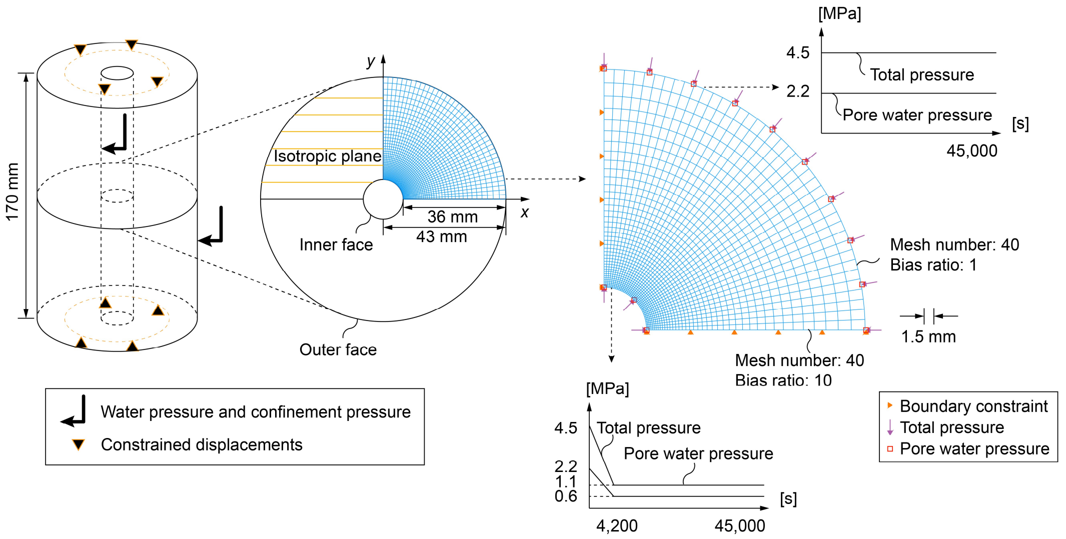

Fig. 14. Geometry, finite element mesh, and boundary conditions of the hollow cylinder test.

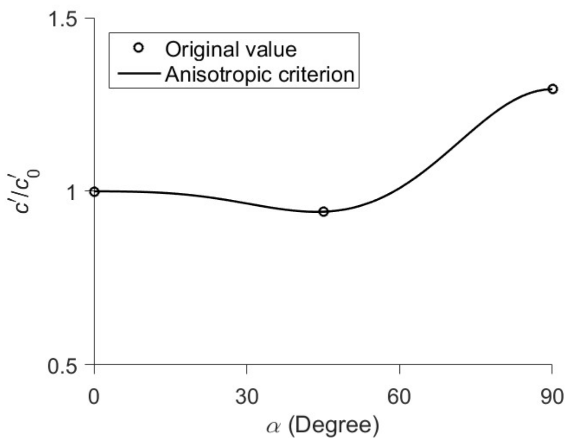

Fig. 15. The proposed anisotropic strength criterion of the cohesion for Boom clay.

Table 2 Set of Boom clay geomechanical, hydraulic and physical parameters in the cross-anisotropic DP model [20].

Parameters	Anisotropic		Isotropic	
Young elastic modulus (MPa)	E'_h	400	E'	300
	E'_v	200		
Poisson ratio (-)	v'_{hh}	0.125	v'	0.125
	v'_{vh}	0.125		
Shear modulus (MPa)	G_v	178		
Initial cohesion (kPa)	c'_0	255	c'_0	255
Initial internal friction angle (◦)	φ'_0	5	φ'_0	5
Strength ratio of cohesion (-)	k_r	1/3	k_r	1/3
Strength ratio of friction angle (-)	k_p	18/5	k_p	18/5
Softening parameters of cohesion (-)	B_S	0.01	B_S	0.01
Hardening parameters of friction angle (-)	B_H	0.01	B_H	0.01
Dilatancy angle (◦)	ψ	0	ψ	0
Parameters $K^{(\alpha)}$ (-)	$K^{(90°)}$	240/255	$K^{(90°)}$	1
	$K^{(45°)}$	330/255	$K^{(45°)}$	1
Internal length (mm)	l	1.5	l	1.5
Permeability (m/s)	k	4×10^{-12}	k	4×10^{-12}
Initial porosity (-)	n_0	0.39	n_0	0.39

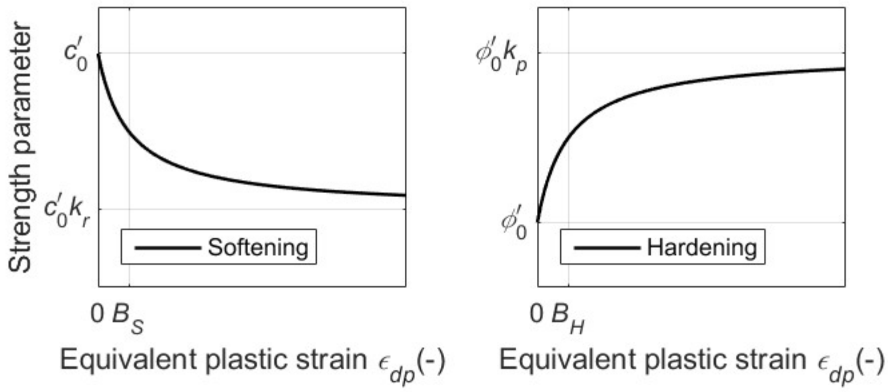

Fig. 16. Softening relation of the cohesion and hardening relation of the internal friction angle of Boom clay.

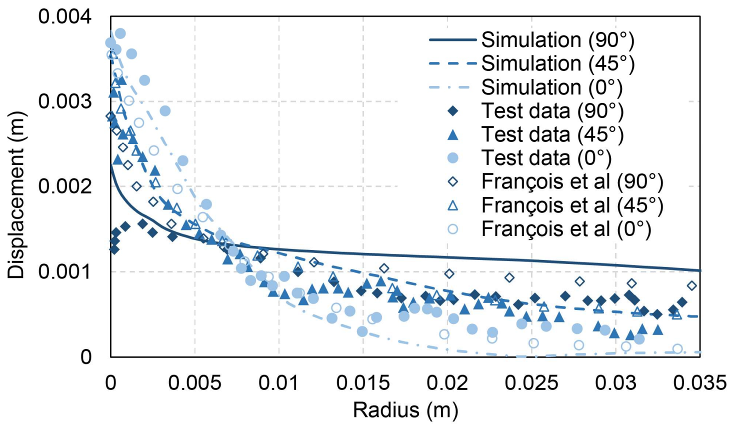

Fig. 17. Comparison of radial displacement in the horizontal (0), 45°, and vertical (90°) directions between the FEA results with a mesh of 60 × 60, the test data [38] and the results obtained by François et al. [20].

A group of finite element simulations is performed in three types of meshes, i.e., 20 × 20, 40 × 40, and 60 × 60. With a 60 × 60 mesh, Fig. 17 shows the simulated radial displacements, the test results [38] and the simulated results [20] for horizontal, 45°, and vertical paths. The displacements of the horizontal and 45° paths obtained by the FEA are close to the other two results. There is a certain deviation between the three displacement curves of the vertical path; however, their trends are the same. Overall, near the inner boundary, the proposed results are closer to the test data compared with those obtained by François et al. [20]. The deviation of the two numerical results may be due to whether the gradient of the yield function involves the component of anisotropic cohesion.

Fig. 18 shows the displacement curves for the three path endpoints located at the inner boundary of the cross-section over the entire simulation time. The analysis process is roughly divided into three stages: unloading, consolidation, and stabilization. In the second half of the unloading stage, i.e., the plastic stage, the three curves of the displacement increase sharply. The displacements in the consolidation stage continue to increase and stabilize in the stabilization stage. Equivalent plastic strain rates of approximately 6500 s obtained by FEA using various meshes are plotted in Fig. 19. The contours of the equivalent plastic strain rate illustrate that the shape of the shear band is identical, although the mesh is coarse in Fig. 19 (a). The widths of the shear bands in Fig. 19 (b) and (c) are close.

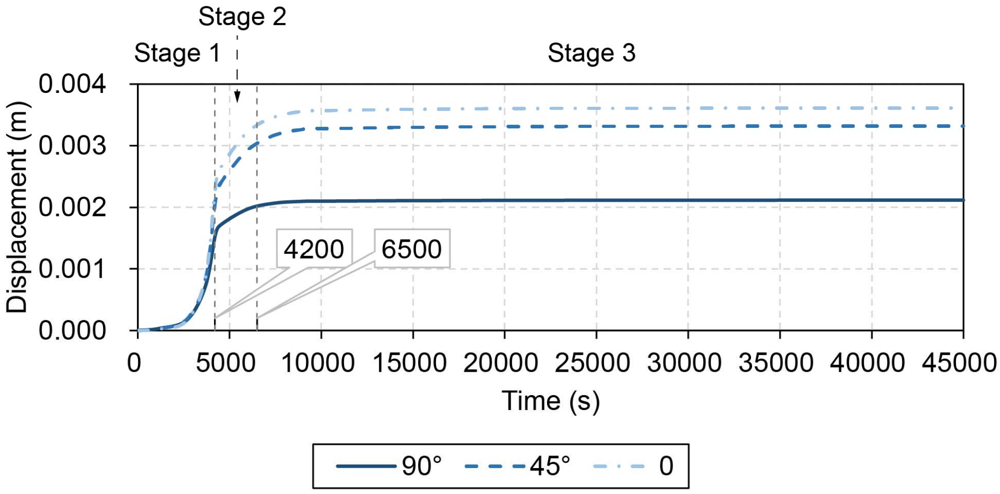

Fig. 18. The displacement curves of the three nodes at the intersection between the inner boundary and the three paths over the entire simulation time.

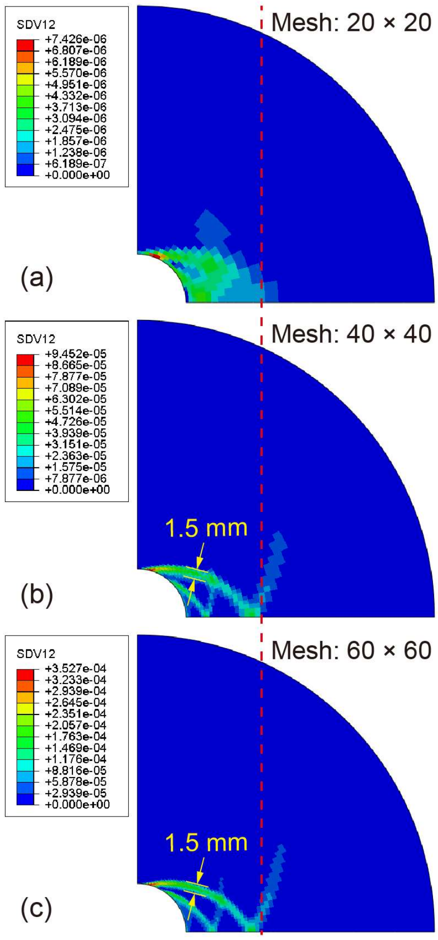

Fig. 19. Rate of the equivalent plastic strain obtained by the finite element analyses with various meshes.

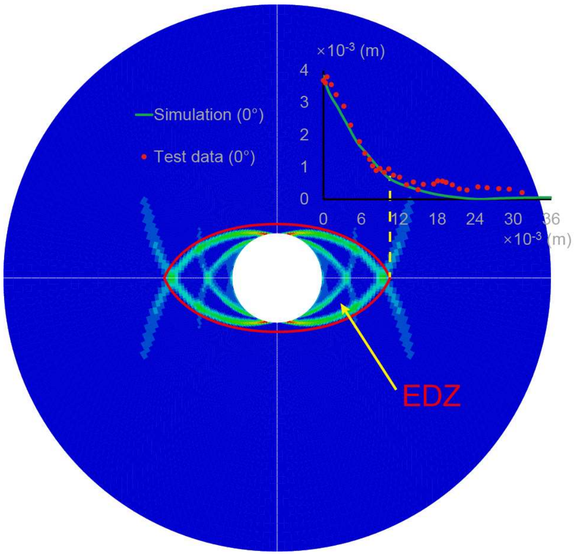

Fig. 20. Predicted EDZ by FEA with the proposed anisotropic DP model.

Fig. 19 (c) is used to assemble the entire cross-section of the sample, as shown in Fig. 20. The shape and boundary of the excavation damaged zone (EDZ) in the hollow cylindrical specimen are determined by the simulated shear band or displacement curve of the horizontal path.

Four cases of anisotropic and isotropic elasticity and anisotropic and isotropic plasticity are analyzed. The results reveal that only anisotropic plasticity can yield eye-shaped strain localization (shear band), as shown in Fig. 21 (a) and (b). Moreover, Fig. 21 (c) shows symmetric strain localization, while Fig. 21 (d) shows axisymmetric strain localization. This analysis can reveal the necessity of the anisotropic strength of Boom clay in the simulation of strain localization.

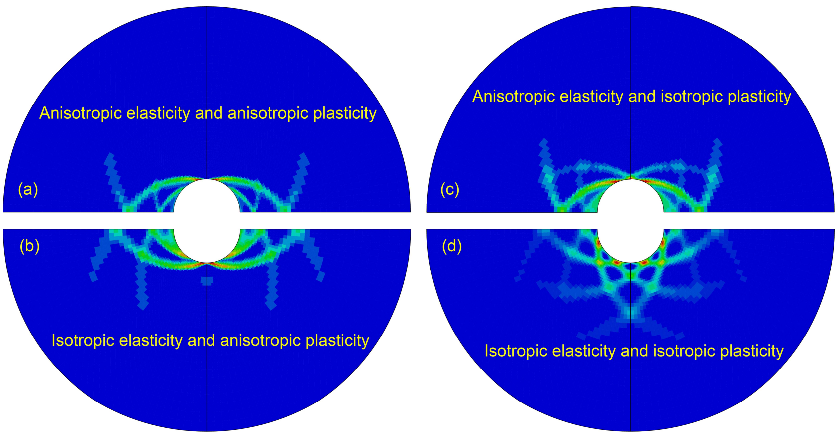

Fig. 22. Rate of the equivalent plastic strain obtained by the finite element analyses with (a) anisotropic elasticity and anisotropic plasticity, (b) isotropic elasticity and anisotropic plasticity, (c) anisotropic elasticity and isotropic plasticity and (d) isotropic elasticity and isotropic plasticity.

Fig. 22 shows the contour of the angle α with anisotropic elasticity and anisotropic plasticity. The angle α varies from zero in the horizontal direction to 90° in the vertical direction. The value of the shear strength changes with α. The clay in the vertical direction provides higher resistance, so the EDZ in the horizontal path is larger.

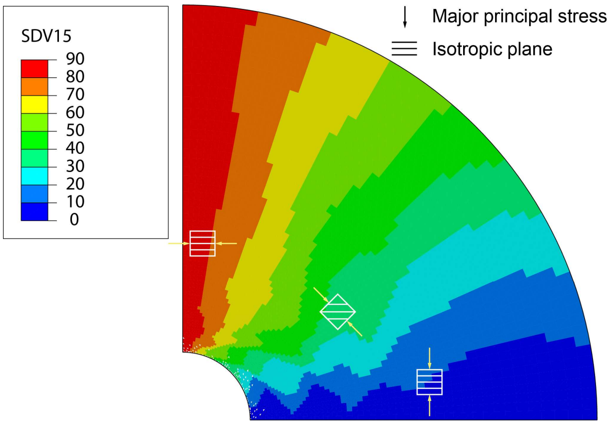

Fig. 22. Contour of the angle between the major principal stress direction and the axis of the isotropic plane.

5 Conclusions

The shear strength of natural clay is highly anisotropic due to the internal structure. An anisotropic failure criterion is proposed for natural clays. An anisotropic variable is used to characterize the relative orientation between the soil fabric and principal stress directions. The model assumes that the cohesion of natural clay (or undrained shear strength) is anisotropic while the friction angle is independent of the loading direction. A DP model with the anisotropic yield criterion has been used to model strain localization in natural clays.

The stability of an undrained clay slope has been analyzed. The results show that the anisotropic undrained strength affects the shape and location of the failure surface (strain localization) of the slope. In the first case, the percentage difference of the stability number obtained by the FESRM is 42% between $K = 0.5$ and $K = 1.5$. When $K > 1.3$, the shape of the slip surface is shallow. In the second case, with different bedding plane orientations, the percentage difference between the maximum and minimum stability numbers is approximately 27%. At $\beta_b = 45°$, the range of the slip body is larger than that at other angles β_b. These results show that the influence of the strength anisotropy and bedding plane orientation on the undrained slope stability cannot be ignored. The influence on the strain localization leads to different slope reinforcement scheme designs.

The proposed model has been applied to simulate the hollow cylinder test on

Boom clay. The displacement results are closer to the test data observed by the X-ray scan [38] than the results obtained by François et al. [20]. The nonlocal softening regularization method used reduces the mesh sensitivity. Furthermore, the rate of the equivalent plastic strain simulated by the nonlocal strain method can be taken to represent the EDZ in the sample. The range of the shear band (strain localization) in the test sample is affected by the anisotropic strength of Boom clay. Only anisotropic plasticity can yield eye-shaped strain localization.

Appendix 1: Gradient of the yield function

The gradient of the proposed anisotropic yield function is expressed as

$$\frac{\partial F}{\partial \sigma'_{ij}} = \frac{\partial F}{\partial p'}\frac{\partial p'}{\partial \sigma'_{ij}} + \frac{\partial F}{\partial q}\frac{\partial q}{\partial \sigma'_{ij}} + \frac{\partial F}{\partial A}\frac{\partial A}{\partial \sigma'_{ij}} \tag{26}$$

where

$$\frac{\partial F}{\partial p'} = -m \tag{27}$$

$$\frac{\partial F}{\partial q} = 1 \tag{28}$$

$$\frac{\partial F}{\partial A} = -g(A)[e_1 + 2e_2(1+A) + 3e_3(1+A)^2]\frac{mc'_0}{\tan\varphi'} \tag{29}$$

$$\frac{\partial p'}{\partial \sigma'_{ij}} = \frac{1}{3}\begin{Bmatrix} 1 \\ 1 \\ 1 \\ 0 \\ 0 \\ 0 \end{Bmatrix} \tag{30}$$

$$\frac{\partial q}{\partial \sigma'_{ij}} = \frac{3}{2q}\begin{Bmatrix} s_x \\ s_y \\ s_z \\ 2\tau_{xy} \\ 2\tau_{xz} \\ 2\tau_{yz} \end{Bmatrix} \tag{31}$$

$$\frac{\partial A}{\partial \sigma'_{ij}} = \frac{1}{2q}\begin{Bmatrix} 1 \\ -2 \\ 1 \\ 0 \\ 0 \\ 0 \end{Bmatrix} + \frac{A}{q}\frac{\partial q}{\partial \sigma'_{ij}} \tag{32}$$

Acknowledgements This work was funded by the Fundamental Research Funds for the Central Universities (Grant No. N2101009). The first author gratefully acknowledges the financial support provided by the China Scholarship Council (CSC No. 201906085065).

Data availability The datasets generated and analyzed during the current study are available from the corresponding author on reasonable request.

References

1. ABAQUS. (2017). ABAQUS Documentation. Providence, RI, USA: Systèmes Dassault.
2. Banerjee PK, Yousif NB (1986) A plasticity model for the mechanical behaviour of anisotropically consolidated clay. Int J Numer Anal Methods Geomech 10(5):521-541. https://doi.org/10.1002/nag.1610100505
3. Belytschko T, Liu WK, Moran B. (2001). Nonlinear finite element for continua and structures (1st ed.). New York: John Wiley & Sons Ltd.
4. Bernier F, Li XL, Bastiaens W (2007) Twenty-five years' geotechnical observation and testing in the Tertiary Boom Clay formation. Géotechnique 57(2):229-237. https://doi.org/10.1680/geot.2007.57.2.229
5. Bertrand F, Collin F (2017) Anisotropic modelling of Opalinus Clay behaviour: From triaxial tests to gallery excavation application. J Rock Mech Geotech Eng 9(3):435-448. https://doi.org/10.1016/j.jrmge.2016.12.005
6. Borja RI, Yin Q, Zhao Y (2020) Cam-Clay plasticity. Part IX: On the anisotropy, heterogeneity, and viscoplasticity of shale. Comput Methods Appl Mech Eng 360:112695. https://doi.org/10.1016/j.cma.2019.112695
7. Brosse AM, Jardine RJ, Nishimura S (2017) The undrained shear strength anisotropy of four Jurassic to Eocene stiff clays. Géotechnique 67(8):653-671. https://doi.org/10.1680/jgeot.15.P.227
8. Casagrande A, Carillo N (1944) Shear failure of anisotropic materials. Journal of the Boston Society of Civil Engineers 31:74-87.
9. Chen WF, Snitbhan N, Fang HY (1975) Stability of slopes in anisotropic, nonhomogeneous soils. Can Geotech J 12(1):146-152. https://doi.org/10.1139/t75-014
10. Conesa S, Mánica M, Gens A, Huang Y (2019) Numerical simulation of the undrained stability of slopes in anisotropic fine-grained soils. Geomechanics and Geoengineering: An International Journal 14(1):18-29. https://doi.org/10.1080/17486025.2018.1490460
11. Crook AJ, Yu J, Willson SM. (2002). Development of an orthotropic 3D elastoplastic material model for shale. SPE/ISRM Rock Mechanics Conference.
12. Dafalias YF (1986) Anisotropic critical state soil plasticity model. Mech Res Commun 13(6):341-347. https://doi.org/10.1016/0093-6413(86)90047-9
13. Dafalias YF, Manzari MT, Papadimitriou AG (2006) SANICLAY: simple

anisotropic clay plasticity model. Int J Numer Anal Methods Geomech 30(12):1231-1257. https://doi.org/10.1002/nag.524

14. Dafalias YF, Papadimitriou AG, Li XS (2004) Sand plasticity model accounting for inherent fabric anisotropy. J Eng Mech 130(11):1319-1333. https://doi.org/10.1061/(ASCE)0733-9399(2004)130:11(1319)
15. D'Ignazio M, Länsivaara TT, Jostad HP (2017) Failure in anisotropic sensitive clays: finite element study of Perniö failure test. Can Geotech J 54(7):1013-1033. https://doi.org/10.1139/cgj-2015-0313
16. Dong W, Xia J (2008) Slope stability analysis by finite elements considering strength anisotropy. Rock Soil Mech 29(3):667-672. [In Chinese]
17. Drucker DC, Prager W (1952) Soil mechanics and plastic analysis or limit design. Q Appl Math 10(2):157-165. https://doi.org/10.1090/qam/48291
18. Duncan JM, Seed HB (1966) Anisotropy and stress reorientation in clay. Journal of the Soil Mechanics and Foundations Division 92(5):21-50. https://doi.org/10.1061/JSFEAQ.0000909
19. Duveau G, Shao JF, Henry JP (1998) Assessment of some failure criteria for strongly anisotropic geomaterials. Mechanics of Cohesive‐frictional Materials: An International Journal on Experiments, Modelling and Computation of Materials and Structures 3(1):1-26.
20. François B, Labiouse V, Dizier A, Marinelli F, Charlier R, Collin F (2014) Hollow cylinder tests on Boom clay: Modelling of strain localization in the anisotropic excavation damaged zone. Rock Mech Rock Eng 47(1):71-86. https://doi.org/10.1007/s00603-012-0348-5
21. Galavi V, Schweiger HF (2010) Nonlocal multilaminate model for strain softening analysis. Int J Geomech 10(1):30-44. https://doi.org/10.1061/(ASCE)1532-3641(2010)10:1(30)
22. Gao Z, Zhao J, Yao Y (2010) A generalized anisotropic failure criterion for geomaterials. Int J Solids Struct 47(22-23):3166-3185. https://doi.org/10.1016/j.ijsolstr.2010.07.016
23. Gao Z, Zhao J (2012) Efficient approach to characterize strength anisotropy in soils. J Eng Mech 138(12):1447-1456. https://doi.org/10.1061/(ASCE)EM.1943-7889.0000451
24. Gao Z, Li X, Lu D (2022) Nonlocal regularization of an anisotropic critical state model for sand. Acta Geotech 17(2):427-439. https://doi.org/10.1007/s11440-021-01236-3
25. Gao Z, Zhao J, Li X (2021) The deformation and failure of strip footings on anisotropic cohesionless sloping grounds. Int J Numer Anal Methods Geomech

45(10):1526-1545. https://doi.org/10.1002/nag.3212

26. Graham J, Houlsby GT (1983) Anisotropic elasticity of a natural clay. Géotechnique 33(2):165-180. https://doi.org/10.1680/geot.1983.33.2.165
27. Griffiths DV, Lane PA (1999) Slope stability analysis by finite elements. Géotechnique 49(3):387-403. https://doi.org/10.1680/geot.1999.49.3.387
28. Grimstad G, Andresen L, Jostad HP (2012) NGI-ADP: Anisotropic shear strength model for clay. Int J Numer Anal Methods Geomech 36(4):483-497. https://doi.org/10.1002/nag.1016
29. Hill R (1948) A theory of the yielding and plastic flow of anisotropic metals. Proceedings of the Royal Society of London. Series A. Mathematical and Physical Sciences 193(1033):281-297.
30. Ip SCY, Choo J, Borja RI (2021) Impacts of saturation-dependent anisotropy on the shrinkage behavior of clay rocks. Acta Geotech 16(11):3381-3400. https://doi.org/10.1007/s11440-021-01268-9
31. Ip SCY, Borja RI (2022) Evolution of anisotropy with saturation and its implications for the elastoplastic responses of clay rocks. Int J Numer Anal Methods Geomech 46(1):23-46. https://doi.org/https://doi.org/10.1002/nag.3289
32. Jin Y, Yin Z (2022) Two-phase PFEM with stable nodal integration for large deformation hydromechanical coupled geotechnical problems. Comput Methods Appl Mech Eng 392:114660. https://doi.org/10.1016/j.cma.2022.114660
33. Jin Y, Yin Z, Zhou X, Liu F (2021) A stable node-based smoothed PFEM for solving geotechnical large deformation 2D problems. Comput Methods Appl Mech Eng 387:114179. https://doi.org/10.1016/j.cma.2021.114179
34. Jin YF, Yin ZY (2020) Enhancement of backtracking search algorithm for identifying soil parameters. Int J Numer Anal Methods Geomech 44(9):1239-1261. https://doi.org/10.1002/nag.3059
35. Kavvadas M. (1982). Non-linear consolidation around driven piles in clays. Massachusetts Institute of Technology.
36. Kontoe S, Summersgill FC, Potts DM, Lee Y (2022) On the effectiveness of slope-stabilising piles for soils with distinct strain-softening behaviour. Géotechnique 72(4):309-321. https://doi.org/10.1680/jgeot.19.P.386
37. Krabbenhøft K, Galindo Torres SA, Zhang X, Krabbenhøft J (2019) AUS: Anisotropic undrained shear strength model for clays. Int J Numer Anal Methods Geomech 43(17):2652-2666. https://doi.org/10.1002/nag.2990
38. Labiouse V, Sauthier C, You S (2014) Hollow cylinder simulation experiments of galleries in Boom clay formation. Rock Mech Rock Eng 47(1):43-55. https://doi.org/10.1007/s00603-012-0332-0

39. Ladd CC (1991) Stability evaluation during staged construction. Journal of Geotechnical Engineering 117(4):540-615. https://doi.org/10.1061/(ASCE)0733-9410(1991)117:4(540)
40. Lade PV, Nam J, Hong WP (2008) Shear banding and cross-anisotropic behavior observed in laboratory sand tests with stress rotation. Can Geotech J 45(1):74-84. https://doi.org/10.1139/T07-078
41. Liu S, Su Z, Li M, Shao L (2020) Slope stability analysis using elastic finite element stress fields. Eng Geol 273:105673. https://doi.org/10.1016/j.enggeo.2020.105673
42. Liu SY, Shao LT, Li HJ (2015) Slope stability analysis using the limit equilibrium method and two finite element methods. Comput Geotech 63:291-298. https://doi.org/10.1016/j.compgeo.2014.10.008
43. Lo KY (1965) Stability of slopes in anisotropic soils. Journal of the Soil Mechanics and Foundations Division 91(4):85-106. https://doi.org/10.1061/JSFEAQ.0000778
44. Mánica MA, Gens A, Vaunat J, Armand G, Vu M (2021) Numerical simulation of underground excavations in an indurated clay using non-local regularisation. Part 1: formulation and base case. Géotechnique 0(0):1-21. https://doi.org/10.1680/jgeot.20.P.246
45. Nova R (1980) The failure of transversely isotropic rocks in triaxial compression. International Journal of Rock Mechanics and Mining Sciences & Geomechanics Abstracts 17(6):325-332.
46. Oda M, Nakayama H (1989) Yield function for soil with anisotropic fabric. J Eng Mech 115(1):89-104. https://doi.org/doi:10.1061/(ASCE)0733-9399(1989)115:1(89)
47. Pardoen B, Seyedi DM, Collin F (2015) Shear banding modelling in cross-anisotropic rocks. Int J Solids Struct 72:63-87. https://doi.org/10.1016/j.ijsolstr.2015.07.012
48. Pariseau WG. (1968). Plasticity theory for anisotropic rocks and soil. The 10th US Symposium on Rock Mechanics (USRMS).
49. Pietruszczak S, Mroz Z (2000) Formulation of anisotropic failure criteria incorporating a microstructure tensor. Comput Geotech 26(2):105-112. https://doi.org/10.1016/S0266-352X(99)00034-8
50. Potts DM, Dounias GT, Vaughan PR (1990) Finite element analysis of progressive failure of Carsington embankment. Géotechnique 40(1):79-101. https://doi.org/10.1680/geot.1990.40.1.79
51. Sachan A, Penumadu D (2007) Strain localization in solid cylindrical clay

specimens using digital image analysis (DIA) technique. Soils Found 47(1):67-78. https://doi.org/10.3208/sandf.47.67

52. Seah TH. (1990). Anisotropy of resedimented Boston blue clay. Massachusetts Institute of Technology.

53. Semnani SJ, White JA, Borja RI (2016) Thermoplasticity and strain localization in transversely isotropic materials based on anisotropic critical state plasticity. Int J Numer Anal Methods Geomech 40(18):2423-2449. https://doi.org/10.1002/nag.2536

54. Sergeyev YM, Grabowska-Olszewska B, Osipov VI, Sokolov VN, Kolomenski YN, Anonymous (1980) The classification of microstructures of clay soils. J Microsc 120(3):237-260. https://doi.org/10.1111/j.1365-2818.1980.tb04146.x

55. Su SF, Liao HJ (1999) Effect of strength anisotropy on undrained slope stability in clay. Géotechnique 49(2):215-230. https://doi.org/10.1680/geot.1999.49.2.215

56. Summersgill FC, Kontoe S, Potts DM (2017) On the use of nonlocal regularisation in slope stability problems. Comput Geotech 82:187-200. https://doi.org/10.1016/j.compgeo.2016.10.016

57. Summersgill FC, Kontoe S, Potts DM (2017) Critical assessment of nonlocal strain-softening methods in biaxial compression. Int J Geomech 17(7):4017006. https://doi.org/10.1061/(ASCE)GM.1943-5622.0000852

58. Summersgill FC, Kontoe S, Potts DM (2018) Stabilisation of excavated slopes in strain-softening materials with piles. Géotechnique 68(7):626-639. https://doi.org/10.1680/jgeot.17.P.096

59. Tang H, Wei W, Liu F, Chen G (2020) Elastoplastic Cosserat continuum model considering strength anisotropy and its application to the analysis of slope stability. Comput Geotech 117:103235. https://doi.org/10.1016/j.compgeo.2019.103235

60. Tang H, Wei W, Song X, Liu F (2021) An anisotropic elastoplastic Cosserat continuum model for shear failure in stratified geomaterials. Eng Geol 293:106304. https://doi.org/10.1016/j.enggeo.2021.106304

61. Terzaghi K, Peck RB, Mesri G. (1996). Soil Mechanics in Engineering Practice (3rd ed.). New York: John Wiley & Sons, Inc.

62. Vitone C, Viggiani G, Cotecchia F, Hall SA (2013) Localized deformation in intensely fissured clays studied by 2D digital image correlation. Acta Geotech 8(3):247-263. https://doi.org/10.1007/s11440-013-0208-9

63. Wheeler SJ, Näätänen A, Karstunen M, Lojander M (2003) An anisotropic elastoplastic model for soft clays. Can Geotech J 40(2):403-418. https://doi.org/10.1139/t02-119

64. Whittle AJ, Kavvadas MJ (1994) Formulation of MIT-E3 constitutive model for overconsolidated clays. Journal of Geotechnical Engineering 120(1):173-198. https://doi.org/10.1061/(ASCE)0733-9410(1994)120:1(173)
65. Yao Y, Lu D, Zhou A, Zou B (2004) Generalized non-linear strength theory and transformed stress space. Science in China Series E: Technological Sciences 47(6):691-709. https://doi.org/10.1360/04ye0199
66. Yin Z, Chang CS (2009) Non-uniqueness of critical state line in compression and extension conditions. Int J Numer Anal Methods Geomech 33(10):1315-1338. https://doi.org/10.1002/nag.770
67. Yin Z, Hattab M, Hicher P (2011) Multiscale modeling of a sensitive marine clay. Int J Numer Anal Methods Geomech 35(15):1682-1702. https://doi.org/10.1002/nag.977
68. Yin Z, Chang CS, Hicher P, Karstunen M (2009) Micromechanical analysis of kinematic hardening in natural clay. Int J Plast 25(8):1413-1435. https://doi.org/10.1016/j.ijplas.2008.11.009
69. Yin Z, Chang CS, Karstunen M, Hicher P (2010) An anisotropic elastic–viscoplastic model for soft clays. Int J Solids Struct 47(5):665-677. https://doi.org/10.1016/j.ijsolstr.2009.11.004
70. Yin Z, Jin Y, Shen JS, Hicher P (2018) Optimization techniques for identifying soil parameters in geotechnical engineering: Comparative study and enhancement. Int J Numer Anal Methods Geomech 42(1):70-94. https://doi.org/10.1002/nag.2714
71. Yuan R, Yu H, Hu N, He Y (2018) Non-coaxial soil model with an anisotropic yield criterion and its application to the analysis of strip footing problems. Comput Geotech 99:80-92. https://doi.org/10.1016/j.compgeo.2018.02.022
72. Zhao Y, Semnani SJ, Yin Q, Borja RI (2018) On the strength of transversely isotropic rocks. Int J Numer Anal Methods Geomech 42(16):1917-1934. https://doi.org/10.1002/nag.2809
73. Zhao Y, Borja RI (2022) A double-yield-surface plasticity theory for transversely isotropic rocks. Acta Geotech 17(11):5201-5221. https://doi.org/10.1007/s11440-022-01605-6